Eur. Phys. J. A **27**, 325–340 (2006)
DOI 10.1140/epja/i2006-10006-0

THE EUROPEAN PHYSICAL JOURNAL A

Lifetimes and side-feeding population of the yrast band levels in ^{131}La

E. Grodner[1,a], A.A. Pasternak[2], Ch. Droste[1], T. Morek[1], J. Srebrny[1], J. Kownacki[4], W. Płóciennik[3†], A.A. Wasilewski[3], M. Kowalczyk[1,4], M. Kisieliński[3,4], R. Kaczarowski[3], E. Ruchowska[3], A. Kordyasz[4], and M. Wolińska[4]

[1] Nuclear Physics Division, IEP, Warsaw University, Hoża 69, 00-681 Warsaw, Poland
[2] Cyclotron Laboratory, A.F. Ioffe Physical Technical Institute, 194021, St.-Petersburg, Russia
[3] The A. Sołtan Institute for Nuclear Studies, 05-400 Świerk, Poland
[4] Heavy Ion Laboratory, Warsaw University, Warsaw, Poland

Received: 6 February 2006 /
Published online: 12 April 2006 –
Communicated by D. Schwalm

Abstract. Lifetimes of yrast levels with spins $I^\pi = 23/2^-$–$43/2^-$ in ^{131}La populated in the ^{122}Sn(^{14}N, 5n) reaction at a beam energy of 70 MeV are measured by the Doppler Shift Attenuation method. A model of side-feeding population is presented. The model parameters are determined in an experiment based on the lineshape of γ-transitions from two highest spin levels and from the intensity distribution along the yrast band. The properties of the $h_{11/2}$ band in ^{131}La are compared with the theoretical predictions obtained in the framework of the Core-Quasi-Particle Coupling and the self-consistent Total Routhian Surface models.

PACS. 21.10.Tg Lifetimes – 21.60.Ev Collective models – 27.60.+j $90 \leq A \leq 149$

1 Introduction

The results of recent experiments (see [1] and references quoted therein) suggest the presence of chiral bands in the odd-odd ^{132}La nucleus. These bands and the similar ones found in the neighbouring odd-odd nuclei with $A \approx 130$ are based on the $\pi h_{11/2} \bigotimes \nu h^{-1}_{11/2}$ configuration. Starosta *et al.* [1] described the chiral bands in ^{132}La in terms of the Core-Particle-Hole Coupling model. As an input to this model the parameters of the triaxial core were fitted to reproduce the properties of the neighbouring even-even and odd-A nuclei. The basic idea of our experiment was to measure nuclear level lifetimes in the yrast band of ^{131}La which is based on a $\pi h_{11/2}$ configuration and thus to obtain input data for the model. The level scheme of ^{131}La is known from ref. [2]. The lifetimes of the $15/2^-_1$, $19/2^-_1$, $23/2^-_1$, $27/2^-_1$ and $31/2^-_1$ states belonging to the $h_{11/2}$ band of ^{131}La were measured [3] by using the Recoil Distance Method (RDM). Due to the limitations of this method the short lifetimes ($\tau < 1$ ps) of the $27/2^-_1$ and $31/2^-_1$ states were determined with very large ($\approx 80\%$) uncertainties, which makes comparison of the high-spin experimental data with the theoretical predictions difficult.

In the present work (whose preliminary results were published in ref. [4]) we used the Doppler Shift Attenuation Method (DSAM) [5,6]. This method is suitable for measuring sub-picosecond nuclear level lifetimes. The lifetimes were determined from the shapes of the γ-lines, account being taken of the reaction kinematics, the de-excitation process of compound nuclei, the slowing-down process of recoils in the target and the geometry of the experimental setup. The experimental techniques, data analysis, discussion of the side-feeding and results of the lifetime measurement are described in sects. 2, 3, 4 and 5, respectively. Some new methods of data evaluation by the DSA method are presented in sect. 3 and in the appendices. Theoretical calculations made in the framework of the Core-Quasi-Particle Coupling model and of the Total Routhian Surface model are given in sect. 6.

2 Experimental

The excited states in ^{131}La were populated in the ^{122}Sn(^{14}N, 5n)^{131}La reaction. The ^{14}N beam of energy 70 MeV was provided by the U-200P cyclotron of the Heavy Ion Laboratory of the Warsaw University. The thickness of the ^{122}Sn target was 10 mg/cm^2. About 10^8 γ-γ coincident events were collected by the OSIRIS II array consisting of 10 Compton-suppressed HPGe de-

[a] e-mail: egrodner@npdoxp.fuw.edu.pl
[†] Deceased.

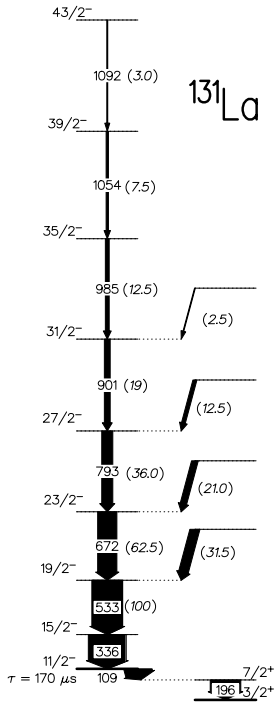

Fig. 1. Partial level scheme of ^{131}La. Numbers in parentheses are the relative intensities given with an accuracy of 5–10%. All transition intensities (in italics) are given for the ^{122}Sn(^{14}N, 5n) reaction at a beam energy of 70 MeV on a thick target. The intensities shown on the right are the sums of intensities of the observed γ-transitions coming from other bands.

tectors with efficiency from 20% to 40% (relative to a standard $3'' \times 3''$ NaI(Tl) scintillator). The Ge detectors were placed at angles θ equal to 25°, ±38°, 63°, ±90°, 117°, ±142° and 155° with respect to the beam axis. The data were sorted off-line into several γ-γ matrices containing events from a specified detector at one axis and events from all the remaining detectors at the second axis. The part of the level scheme of ^{131}La used in the present analysis is shown in fig. 1.

3 Data analysis

3.1 General features of the method

The lifetime analysis was carried out by using the programs COMPA, GAMMA and SHAPE. This software includes the Monte Carlo simulation of production and slowing-down of recoils as well as γ-quanta emission and registration. In the present work we used the upgraded version of the old program [7]. When heavy ions are used the following problems arise:

1) In compound-nucleus reactions induced by heavy ions the states with large angular momenta are populated. Therefore, the side-feeding time (τ_{sf}) may be comparable with the analysed level lifetime τ and is characterized by non-exponential distribution. So, the complicated side-feeding process should not be described simply by a single value of τ_{sf}.

2) For long cascades, the calculation of lineshape as a superposition of many components leads to a large error, which drastically increases if the values of the τ_i inside cascade are almost equal. In this case the probability that decay occurs in the t, $t + \mathrm{d}t$ interval is described by the law

$$\mathrm{d}P(t)/\mathrm{d}t = \sum_{i=1}^{n} \left(\prod_{\substack{k=1 \\ k \neq i}}^{n} \frac{\tau_i}{\tau_i - \tau_k} \right) \frac{1}{\tau_i} \exp\left(-\frac{t}{\tau_i}\right) \quad (1)$$

and consists of large positive and large negative summands.

The well-known code LINESHAPE [8] attempts to solve problem 1) by introducing an artificial level cascade (5 levels) for each analysed state to replace the complex side-feeding pattern. These levels decay via stretched $E2$ transitions with a rotation-like behaviour and are described by one parameter (effective quadrupole moment Q_{sf} or effective side-feeding lifetime τ_{sf}) which is different for each analysed level. This parameter should be extracted during lineshape analysis simultaneously with τ. This approach is questionable (at least in the case of not well-deformed nuclei) especially if τ_{sf} significantly exceeds τ (for instance see [9]).

In the present version of our program (already applied to analyse the experiments performed with the GASP and EUROBALL IV arrays [10–12]) all cascades which feed the level of interest, starting from the entry states, are directly included in the Monte Carlo simulation and lineshape calculation. The model of side-feeding used in our approach is based on the modern knowledge of population and decay of the entry states. Details of the model are given in appendix C. The side-feeding is described by several parameters. They are the same for all levels of interest and can be determined from lineshape analysis and also from other independent experimental data like multiplicity distributions or side-feeding intensities. In our program the number of levels and decay paths in the feeding cascade is practically unlimited since one hundred levels and 10^5 paths can be taken into account. Moreover, the level scheme analysis and path identification are performed automatically since all experimental branching ratios are taken into account. Any condition of gating is realised by the use of the Monte Carlo techniques (see sect. 3.2 and appendix A). Our approach using the WGTB method (Wide Gate set on Transition Below the level of interest method) based on side-feeding cascade calculations is to some extent model dependent since specific structural effects which might influence the feeding of the analysed level are not accounted for. In the present experiment the influence of specific structural effects is not substantial since the side-feeding model reproduces well the distribution of intensity and the relative side-feeding intensity population along the yrast band. These observables depend on the feeding time distribution probability. The agreement of these quantities with experimental ones shows that for studied levels the feeding time distribution is calculated properly. A more detailed description of the problem is given in sects. 3.4, 4.1, 4.2. In the case of ^{131}La

it is proved by lifetime analysis of the $31/2^-$ level that the model of side-feeding, whose parameters were experimentally determined, describes well the feeding time distribution of the studied levels. The lifetime of the $31/2^-$ level extracted by using the side-feeding–independent methods (gating above, narrow gate below) give the same result as our approach in which the feeding time is calculated according to the model described in sect. 3.4. This shows that the feeding time distribution of the $31/2^-$ level, given by the model, reproduces the experimental distribution (see sect. 5.2).

3.2 Setting of gates

To avoid systematic errors associated with the cascade and side-feedings one can set a gate on the transition that feeds the level of interest. It limits the feeding to a known path [13]. When the gate is set on the Doppler shifted (flight) component of the feeding transition (partial gate), then the results are low sensitive to the population time since only the fast component of the feeder transition is used for gating. This method is usually called Flight Gate Transition Above (FGTA); in this paper it shall be referred to as "gating above". The "gating above" method may be applied for any γ-transition which feeds the level of interest. The general description of this method, where the Monte Carlo procedures were used, is presented in [10]. In appendix D of ref. [10] the time-velocity correlation connected with the stopping process of recoils is calculated by using formula

$$t(v) = m \int_0^v \left(\frac{\mathrm{d}E}{\mathrm{d}x}(u) \right)^{-1} \mathrm{d}u \,, \qquad (2)$$

where $\mathrm{d}E/\mathrm{d}x$ is the recoil stopping power as a function of velocity u. The Monte Carlo simulated time t_1 of the γ-ray emission (see sect. 3.3) is used to calculate the recoil velocity v (and its projection $v\cos\theta$ on the detector direction) at the moment of γ de-excitation. The time-velocity correlation (given in eq. (2)) and velocity projection are necessary to calculate the Doppler-shifted energy of the γ-quantum registered in the detector

$$E_\gamma = E_{\gamma_0} \left(1 + \cos\theta \frac{v(t_1)}{c} \right) + \Delta E_{random} \,, \qquad (3)$$

where E_{γ_0} is the unshifted energy of the photon and ΔE_{random} is used to describe the influence of the instrumental lineshape, see appendix B in ref. [10]. For the partial gate, set in the energy interval of E_L–E_R, the Monte Carlo event is accepted when $E_L < E_\gamma < E_R$, where E_L and E_R stand for the left- and right-hand limit of the gate. This event represents the case in which the γ-decay (starting from the entry states of the recoil nucleus) fulfils the conditions given by the partial gate. In our case the $31/2$ level was analysed by applying a variant of this technique where the sum of the spectra from all detectors was used for the lifetime extraction. The position and width of the gate were fixed and different parts of the velocity distribution, for each angle, were automatically taken into account in the lineshape calculation.

Another method of avoiding systematic errors associated with cascade and side-feeding, known as "Narrow Gate set on Transition Below" (NGTB), was introduced by Brandolini *et al.* in [14] and has been improved by Petkov *et al.* in [15]. In this method a gate is set on the unshifted component of the transition depopulating the level of interest and the lineshape of the transition feeding the level of interest is analysed. This lineshape is compared with the lineshape measured when the gate is set on the whole line containing the shifted and unshifted components of the depopulating transition. When the gate is set only on the unshifted component of the transition then the Doppler-shifted component of the feeding transition is suppressed. From the degree of suppression, the lifetime of the level can be deduced.

In appendix A a new version of the NGTB method, called in our paper "narrow gate", is described. The method allows us to enlarge the width of the gate set on the unshifted component of the depopulating transitions what increases the statistics of the spectrum. Application of the Monte Carlo calculations to this method has been described in [10]. The $31/2$ level in ^{131}La was analysed by applying this technique too. However, the Wide Gate set on the Transition Below the level of interest (WGTB) method is used as standard. This method will be called "gating below". Often in the "gating below" method the sum of many gates below is used, therefore the statistics of the spectrum can be much larger as compared to the "narrow gate" and "gating above" methods. This is the reason why in our work most of the lifetimes were obtained by applying the "gating below" method. This procedure applied to small arrays (like OSIRIS) is useful also in the case of large arrays (EUROBALL, GAMMASPHERE, GASP) since there are always weak transitions for which the "narrow gate" and "gating above" methods cannot be applied [10–12]. It is worth noting that the "gating above" method is effective only in the case of a sufficiently large Doppler effect shown by feeder transition and that the sensitivity of the "narrow gate" method depends on the lifetimes of both analysed levels: level of interest and level above. In general, the application of the "gating below" method results in a significant increase of the number of lifetimes which can be extracted, provided the side and cascade feedings are properly taken into account.

3.3 Cascade feeding

In the "gating below" method the cascade feeding from known discrete states makes the lifetime determination difficult. Generally, the total number of different decay paths in the level scheme that feed the level of interest is $K_{total} = 2^{N-1}$, where N is the number of states above this level and, for example, for $N = 30$, $K_{total} \approx 5 \times 10^8$. Fortunately, only a small number K of paths is realised ($K \ll K_{total}$). A special subroutine of GAMMA analyses the level scheme starting from the top and picks the paths

for which the electromagnetic transitions exist. Each path is identified by the code identification number (k) stored together with the relative intensity R_k of the path. The program GAMMA divides the total number of the Monte Carlo histories M (typically 10^5) into K parts proportional to R_k: $M_k = M \times R_k$. Finally, the program takes into account the all known branches of the cascade feeding. Each path contains transitions from n discrete levels and side-feeding transitions. The simulated time t_1 at which a γ-quantum de-excites the level of interest (its sequence number is defined as unity) is given by equation

$$t_1 = t_{sf} + \sum_{i=2}^{n} t_i \,, \tag{4}$$

where t_i is the simulated time for the corresponding transition from level i and t_{sf} is the simulated time at which the feeding reaches the upper level ($n = i$) in the band. Each t_i is calculated from the formula $t_i = \tau_i \ln(1/\zeta)$, where ζ is a random number evenly distributed in the interval $(0, 1)$.

The resulting time distribution is fully equivalent to the complex superposition of the exponential function in eq. (1). At time t_1 the recoil velocity and corresponding Doppler shifts are simulated for each detector. The described Monte Carlo method of cascade feeding simulation is superior in accuracy to the analytical calculation, and holds for any combination of lifetimes τ_i in the cascade, even if some of them are equal.

When the level scheme is well established and the intensity is large enough, the best way of applying the "gating below" method is step-by-step extraction of lifetimes, starting from the upper levels and taking into account all feeding cascades. Uncertainties in the lifetimes of the upper levels do not strongly affect the lifetime determination of the level of interest. Namely, the following correlation takes place along the path: the increase (decrease) of the lifetime (τ_u) of the upper level leads to the decrease (increase) of the lifetime (τ_b) of the level below, etc. This compensates partly the influence of the τ_u and τ_b uncertainties on the lifetime of levels of interest [16]. The time-dependent decay function $\mathrm{d}P(t)/\mathrm{d}t$ for each feeding path is the superposition of exponents but in some cases can be roughly replaced by one exponent with the effective value of lifetime τ_{eff}. The definition of τ_{eff} by using the $P(t)$-function is given in appendix B. Usually, τ_{eff} can be roughly estimated as the sum of lifetimes in the stretched cascade (including the level of interest). In the case of DSA, if τ_{eff} is comparable or larger than the recoil's stopping time t_{stop} (see appendix B), the observed Doppler effect is determined by another effective time τ_{eff}^{DSA}. This effective time can be evaluated by the lineshape analysis under the assumption of one component exponential decay without any cascade and side-feedings. The value τ_{eff}^{DSA} always exceeds τ_{eff}. This can be explained by the fact that in the case of DSAM only the part of the $\mathrm{d}P/\mathrm{d}t$-function during the recoil slowing-down time is important (see appendix B). In the real situation one parameter τ_{eff}^{DSA} is not enough for the proper description of the lineshape. In practice, satisfactory results are obtained if the cascade feeding of the level of interest is reduced to 2–3 transitions. Substitution of the feeder branch by one level with effective feeder lifetime τ_{eff}^{feed} is correct in two cases:

1) $\tau_{eff}^{feed} \ll \tau$. Usually, in this case $\tau_{eff}^{feed} \ll t_{stop}$ and the population of studied level is so fast that its detailed description is not important.

2) $\tau_{eff}^{DSA} \gg t_{stop}$. In this case the cascade feeding contributes mainly to the stop component of the analysed line.

In ^{131}La (fig. 1) there is no information about the side branches for the highest levels and also the information for the lowest levels is probably incomplete. The unknown side branches are included into the side-feeding for these levels. These side-feedings were calculated by the Monte Carlo simulation in the way discussed in sect. 3.4.

We found that the lifetime uncertainties for the upper levels of the yrast band have little effect on the obtained values of the lifetimes of the $23/2^-$ and $27/2^-$ levels. Moreover, the lineshapes of all observed discrete feeding transitions from side bands do not exhibit the Doppler broadening effect. This may be due to their long effective lifetimes. Therefore, for each level all side branches can be substituted by a single transition. It was assumed that their effective lifetime is 2 ± 1 ps. This value is larger than the average recoil's stopping time ($t_{stop}^{av} \approx 1$ ps, see appendix B) and, its uncertainty does not significantly influences the lifetimes of the $23/2^-$ and $27/2^-$ levels.

3.4 Side-feeding

The model of side-feeding, described below, gives not only the feeding time distribution for the levels of interest but also helps to understand better the decay process leading from the entry-state distribution to the studied levels. Figure 2 shows the entry-state plot calculated by using the code COMPA (some details of the calculations are given in appendix C). The maximum of entry-state distribution lies close to the studied levels due to the relatively low angular momenta and large number of evaporated particles (5 neutrons). Therefore, the side-feeding times are

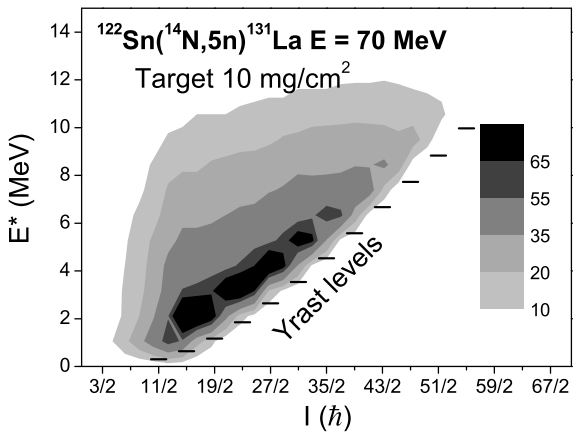

Fig. 2. Entry-state population calculated with the use of the COMPA code for the ^{122}Sn(^{14}N, 5n)^{131}La reaction.

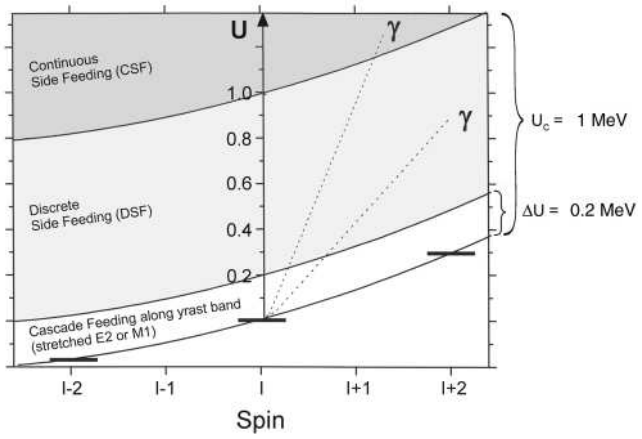

Fig. 3. Excitation energy U above the yrast level at spin I. The three solid lines show: the yrast line, the lines at $\Delta U = 0.2\,\mathrm{MeV}$ and $U_c = 1\,\mathrm{MeV}$ above the yrast state. The type of the side-feeding components depends on the energy U of the last feeder level. If from simulation the last side-feeding transition populates the level located below the $\Delta U = 0.2\,\mathrm{MeV}$ line then this level is regarded as belonging to the yrast band. The energy width $\Delta U = 0.2\,\mathrm{MeV}$ follows from a gap in the level density distribution [42].

expected to be small, which creates favourable condition for the DSAM lifetime measurements. We encountered a similar situation in ^{119}I, ^{118}Te and ^{120}Xe nuclei [7,17,16], which were also populated in a compound-nucleus reaction with low input angular momenta. On the other hand, the entry-state distribution is characterised by a fairly wide spread along the spin axis, which partly reflects the large spread of projectile energy due to the slowing-down process in a thick target. Therefore, γ-cascades leading from entry states to the levels of interest should have both short (related mainly to the cascades of statistical transitions) and long (stretched) components. Moreover, contributions of these components should strongly depend on the analysed level spin. The side-feeding time distributions of the populated level are simulated by a part of the GAMMA program. In this code the side-feeding depends on the energy and spin of the lowest level in the feeder cascade (see fig. 3).

There are two types of side-feeding for the levels lying close to the yrast line:

1) Feeding via decay of the entry states lying at $U > U_C \approx 1\,\mathrm{MeV}$ above the yrast line, *i.e.* from quasi-continuum levels. This feeding can be referred to as Continuum Side-Feeding (CSF).

2) Feeding via decay of discrete levels and rotational bands lying at $\Delta U < U < U_C$. This feeding can be referred to as Discrete Side-Feeding (DSF). The DSF transitions although numerous are not visible due to their low intensities.

The calculations of both CSF and DSF include not only statistical $E1$ transitions and the stretched $E2$ bands with damping effect, but also statistical $M1$ and $E2$ transitions (for details see appendix C). For the case of near-magic nuclei a special hypothesis has been made which allows us to consider the existence of a large amount of particle-hole excitations in the entry-state region which generate magnetic rotational bands with a shear effect [18]. The contributions of statistical and stretched ($E2$ and $M1$) components are different for CSF and DSF. CSF is fast since the energy of the last transition leading to the studied level exceeds 1 MeV. On the other hand, DSF is responsible for the relatively slow component of the side-feeding due to the low transition energy.

The decay paths from each point of the entry region are described by one set of empirical parameters common for all levels. These parameters are: Q_{low}, Q_{high} —effective quadrupole moments of stretched $E2$ cascades in continuum for the low- and high-spin regions, respectively, and S_{MR} —the relative density of stretched magnetic bands in continuum (see appendix C). The parameters can be obtained by fitting simultaneously two different types of data:

1) γ-lineshapes sensitive to the population time distribution of the high spin levels,

2) multiplicity distribution and intensity distribution along the yrast band.

This procedure was applied for the first time for the nearly magic $^{142-146}$Gd nuclei in refs. [18,19]. The parameters of the side-feeding pattern have been obtained from the experimental γ-multiplicity distribution and lineshape analysis of transitions between high-spin states. These parameters were used for the Doppler Shift Attenuation study of lifetimes (refs. [10–12]). In the present work, instead of γ-multiplicity the distribution of intensity and the relative side-feeding population along the yrast band have been used together with the lineshape analysis of high-spin states ($39/2^-$, $43/2^-$) in ^{131}La.

The parameters evaluated in this way were used for the DSA lifetime determination of the yrast levels in ^{131}La. The correctness of the methods used to evaluate the side-feedings pattern is partly proved by the agreement of the lifetime obtained from the lineshape analysis of the $31/2^-$ level by the "gating below" method with those found by the "gating above" and "narrow gate" methods which do not depend on the side-feeding time distribution.

The results of the Monte Carlo simulation of the side-feeding time distribution, including both the CSF and DSF components, are shown in the upper part of fig. 4 which illustrates the complex structure of side-feeding time distribution ($\mathrm{d}P/\mathrm{d}t$). These results disagree with the result of the conventional method where the $\mathrm{d}P/\mathrm{d}t$ distribution is calculated in terms of the one-band model. This model considers several stretched $E2$ transitions characterised by the effective transition quadrupole moment or effective side-feeding time for each studied level. For rough comparison of side-feeding times with the measured lifetimes, the effective side-feeding time τ_{sf} can be defined using the formula (see appendix B):

$$\int_0^{\tau_{sf}} (\mathrm{d}P(t)/\mathrm{d}t)\mathrm{d}t = 1 - e^{-1}. \quad (5)$$

The spin dependences of τ_{sf} have been calculated for CSF as well as for the total side-feeding CSF+DSF by us-

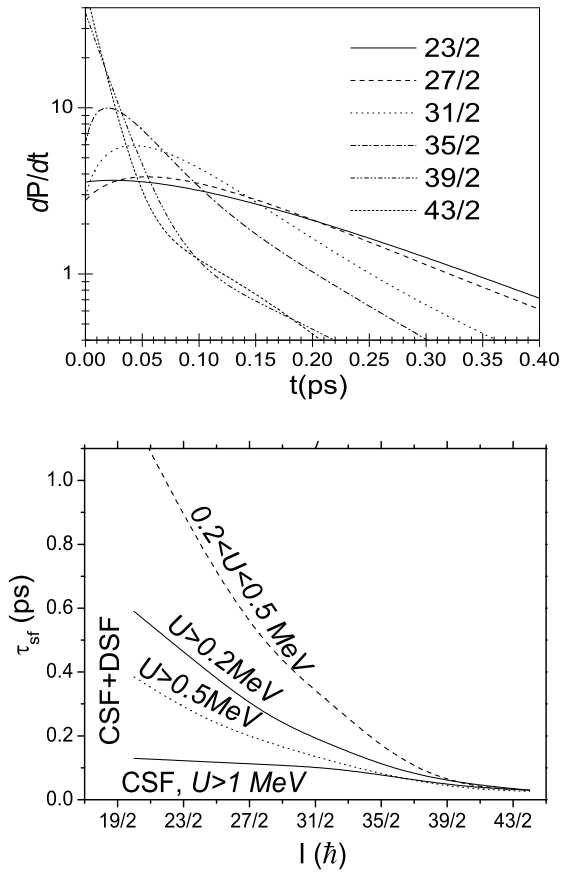

Fig. 4. Upper part: time distribution of the side-feeding population for all studied levels. The results of calculations for experimentally fixed parameters (see sect. 4) are shown. Lower part: the results of model calculation of the effective side-feeding time τ_{sf} as a function of the level spin. The results are shown for various energy positions of the last feeder (see fig. 3) including continuous side-feeding (CSF) and discrete side-feeding (DSF).

ing this definition. The results are shown as two solid lines in the lower part of fig. 4. The difference between these lines grows with decreasing spin. This reflects the increasing contribution of the relatively slow stretched cascades to side-feeding. For low spin levels the part of intensity due to the known feeding bands becomes large (see fig. 1) and two limiting cases can be considered in side-feeding interpretation:

1) all discrete levels up to $U \approx 1\,\mathrm{MeV}$ which feed the level of interest are known. Then only CSF is responsible for the side-feeding and should be taken into account in the τ_{sf} simulation.

2) the unobserved feeder transitions originate from the level at $U > 0.2\,\mathrm{MeV}$. Then CSF+DSF should be taken into account.

In practice, the upper limit of U for discrete side bands U_{obs} can be evaluated from observed level scheme. Then only the part of DSF corresponding to $U > U_{obs}$ should be considered. The dotted line in the bottom panel of fig. 4 corresponds to the case where CSF+DSF with $U > U_{obs} = 0.5\,\mathrm{MeV}$ was taken into account. The dashed line represents the effective feeding time of the $23/2^-$ and $27/2^-$ levels for $U < U_{obs}$. The predicted values of τ_{sf} for these two levels are comparable with the stopping time ($\approx 1\,\mathrm{ps}$). This is the reason why the DSA effective lifetime of the observed side bands feeding the yrast band (see fig. 1) should be of the same order as that predicted by the presented model of side-feeding:

$$\tau_{sf}^{DSA}(\text{side band}) \approx \tau_{sf}(U < 0.5\,\mathrm{MeV}). \qquad (6)$$

The difference between τ_{eff}^{DSA} and τ_{eff} is explained in appendix B. The contributions of the fraction of side-feeding ($U > 0.5\,\mathrm{MeV}$) to the effective side-feeding time should be small and lay between that predicted for CSF ($U > 1\,\mathrm{MeV}$) and that for the full (CSF+DSF) side-feeding (CSF+DSF) ($U > 0.2\,\mathrm{MeV}$) —see fig. 4. The uncertainties of the side-feeding calculations increase with the decreasing value of spin, whereas the contribution of side-feeding to the total feeding intensity becomes small. Finally, the uncertainty of the side-feeding pattern does not affects strongly ($\pm 15\%$) the extracted lifetime.

3.5 Stopping-power parameters

In the present experiment the maximum recoil velocity, for the 5n evaporation reaction, equals $0.0136c$. The stopping-power parameters of La recoils moving in Sn material were measured for this velocity region (experimental details will be published in [20]) using the semithick-target method [7]. The stopping power of recoils is a sum of electronic and nuclear stopping powers described by the three parameters f_e, f_n and ϕ_n [21]. Values of $f_n = 0.83$ and $\phi_n = 1$ were taken to reproduce the nuclear stopping power of Ziegler [22]. With nuclear stopping-power fixed parameters, the value $f_e = 1.0 \pm 0.1$ was obtained from our experiment [20]. The contribution of the inaccuracy of the stopping power to lifetime determination was evaluated as 10%. The uncertainty of the recoil stopping power acts approximately as a multiplicative factor on the τ and $B(E2)$ values and only slightly affects the physical interpretation given in our paper.

4 Results of the side-feeding study

The effective quadrupole moments Q_{low}, Q_{high} and the parameter S_{MR} (which is responsible for the $M1$ stretched cascades) are parameters which have to be extracted from the experiment. The parameter Q_{high} has been extracted from the lineshape analysis of the transitions from the $43/2^-$ and $39/2^-$ states, whereas Q_{low} and S_{MR} from the analysis of the transition intensity distributions.

4.1 Lineshape analysis of transitions from the $43/2^-$ and $39/2^-$ states

As it was said in the previous section the DSA analysis of lineshape of γ-transitions between high-spin states with a

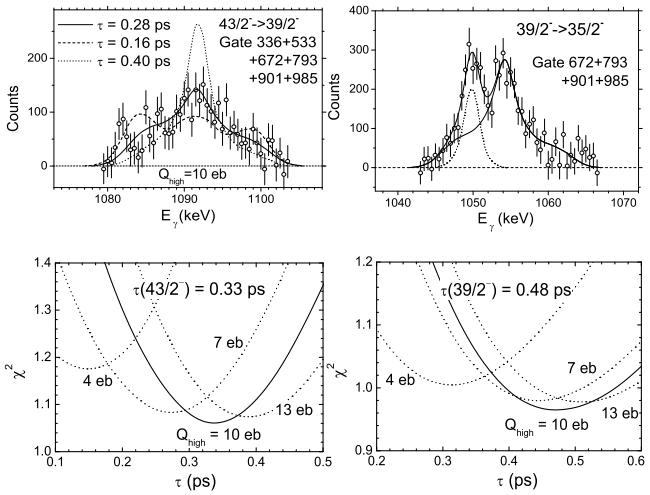

Fig. 5. Upper part: experimental and calculated lineshapes for the 1092 keV ($43/2^-$) and 1054 keV ($39/2^-$) transitions in ^{131}La. The spectra have been summed over 10 Ge detectors. The lineshapes for the $43/2^-$ level are presented for different level lifetimes. In the case of the $39/2^-$ level, the additional peak at 1050 keV (dotted line) corresponds to side transitions $29/2^- \rightarrow 27/2^-$ in ^{131}La. Lower part: χ^2 plots *versus* τ for different Q_{high} values for the $43/2^-$ and $39/2^-$ levels in ^{131}La. Solid lines present plots for the optimal Q_{high} value which in both cases is equal to 10 ± 3 eb.

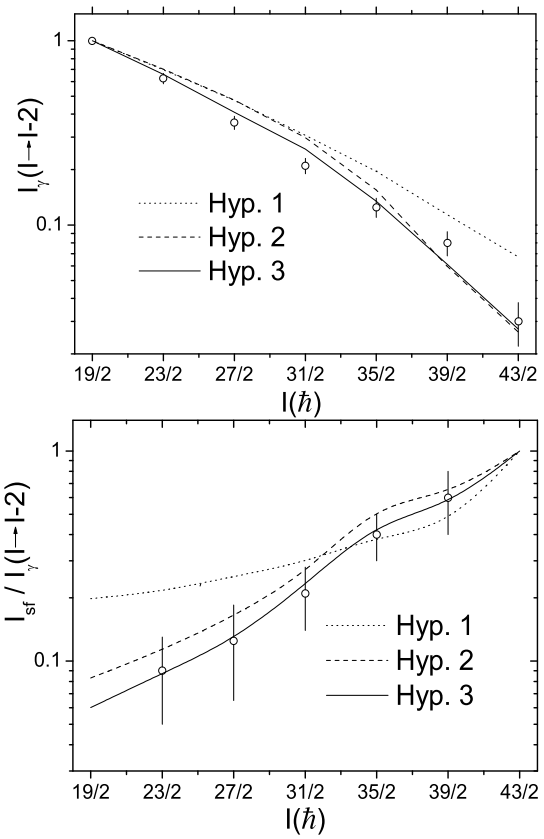

Fig. 6. Upper part: intensity distribution along the yrast line for three hypotheses (see text in sect. 4.2). Lower part: side-feeding intensities normalised to the intensity of $I \rightarrow I-2$ transitions.

large contribution of side-feeding can, in some cases, give simultaneously two quantities —the lifetime (τ) of the corresponding levels and the effective side-feeding time (τ_{sf}) or effective quadrupole moment Q_{high} of the stretched side-feeding cascade. Such a study was performed in the present work to evaluate the parameters which determine side-feeding. Unlike the simple conventional methods, where usually one effective side-feeding band is taken into account for each level, in our approach all cascades starting from each point of the entry-state region are simulated by the Monte Carlo method in lineshape calculations. The parameters of statistical transitions are fixed (see appendix C). Therefore, Q_{high} is the parameter which determines the time distribution of the side-feeding population of the highest spin levels. The value of Q_{high} is expected to be large [23]. According to the model calculation it was assumed that the contribution of stretched $M1$ transitions is not important, because these transitions influence rather the multiplicity distribution than the time distribution. In our case, the decays of the $43/2^-$ and $39/2^-$ levels have been chosen for analysis. This allowed us to determine three quantities: $\tau_{43/2}$, $\tau_{39/2}$ and Q_{high}. The χ^2 plots *versus* τ for different Q_{high} values are shown in the lower part of fig. 5. The optimal value of $Q_{high} = 10 \pm 3$ eb was obtained from both fits. Experimental and calculated lineshapes for the 1092 keV ($43/2^-$) and 1054 keV ($39/2^-$) transitions of ^{131}La are given in the upper part of fig. 5 for the spectra summed over 10 Ge detectors; the calculated lineshapes for various τ and the fixed value of the parameter $Q_{high} = 10$ eb are also shown for the $43/2^-$ level.

4.2 Analysis of the transition intensity distributions

The relatively small Doppler effect and strong cascade feeding make difficult the evaluation of Q_{low} and S_{MR} based on the lineshape analysis for γ-transitions from middle and low spin levels. Therefore, we have determined both parameters from the intensity distribution. Two types of experimental data were analysed:

1) intensities along the yrast line (see fig. 6, upper part);

2) relative side-feeding intensities, *i.e.* relative difference between the intensities of all observed γ-lines depopulating and populating the same level (see fig. 6, lower part).

Data 1) were compared to the results of model calculations which take into account, continuous and discrete side-feedings with $U > 0.2$ MeV (see fig. 3 and fig. 4). Data 2) were compared with the results of model calculations for $U > 0.5$ MeV since the observed side bands are below the limit $U < U_{obs} = 0.5$ MeV. These experimental data depend on sensitivity of the side bands observation. Data 1) are free of this shortcoming.

The calculations were made for three hypotheses. The first one corresponds to the side-feeding pattern with $Q_{high} = 10$ eb (obtained for the 39/2 and 43/2 states). This value is taken for all states (dotted line in fig. 6). Hy-

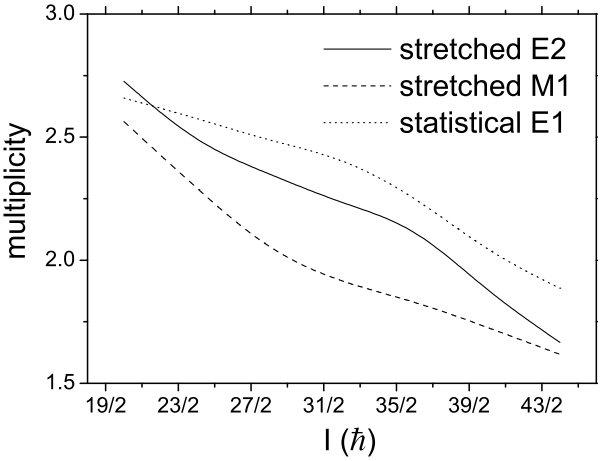

Fig. 7. Contribution of various multipolarities to the total side-feeding γ-multiplicity calculated with parameters fitted to the experimental data (see hypothesis 3 in sect. 4.2).

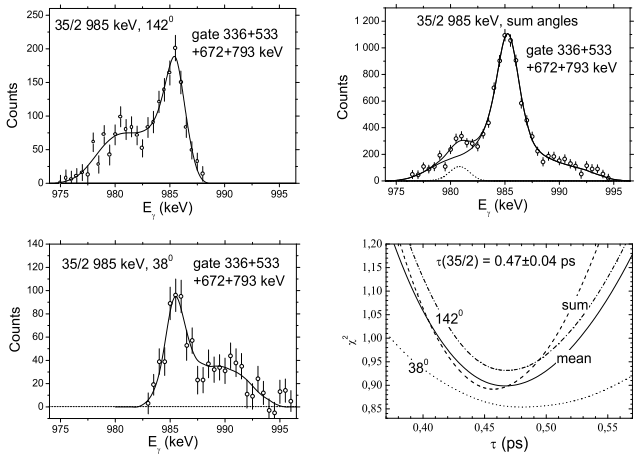

Fig. 8. Lineshape analysis performed by using the "gating below" method for the 985 keV transition depopulating the $35/2^-$ level. The dotted line in the "sum" spectrum (upper right part) shows the background peak. The position of the contamination line in the "sum" spectrum has been found independently and was fixed during fitting. The solid line at the bottom of the right-hand part corresponds to the mean value of χ^2 obtained for different spectra. All χ^2 values are divided by the number of degrees of freedom. Only statistical errors are shown.

pothesis 2 assumes $Q_{high} = 10\,\mathrm{eb}$ for the high-spin region with $I > 21\hbar$ and $Q_{low} = 4.5\,\mathrm{eb}$ for lower spins (dashed line in fig. 6). In both hypotheses $S_{MR} = 0$. It means that $M1$ stretched bands were not taken into account. Hypothesis 3 assumes $Q_{high} = 10\,\mathrm{eb}$ and optimal values of Q_{low} and S_{MR} resulting from the fit to the experimental data: $Q_{low} = 4.5 \pm 0.7\,\mathrm{eb}$, $S_{MR} = 0.06 \pm 0.02$. As can be seen in fig. 6, only calculations performed with hypothesis 3 reproduces well the experimental data. In fig. 7 the contribution from the statistical $E1$ and stretched $E2$ and $M1$ transitions to the total side-feeding multiplicity calculated with parameter of hypothesis 3 is presented. One can see that $M1$ stretched bands play an important role in the side-feeding. In our DSA analysis the parameters Q_{high}, Q_{low} and S_{MR} of hypothesis 3 were used. They are in agreement with the expected values (appendix C).

5 Results of the lifetime study

The final values of lifetimes were determined in the χ^2 fitting procedure applied to the results obtained by different methods (see sect. 3.2) by using spectra "38°", "142°" and "sum" of spectra ("sum") (see notes [d] and [e] in table 1). Each detector (placed at θ) registers γ-quanta in coincidence with all other detectors. It turned out that for this manner of registration the sum of angular correlations can be replaced approximately by the angular distribution: $1 + A_2 P_2(\cos\theta)$ with the A_2 coefficient equal to about 0.3 for pure $E2$ transitions. For summed spectra the efficiency of each detector and the angular-distribution coefficient, being input parameters to the code GAMMA, were taken into account. The side-feeding parameters, identical for all discussed levels, were evaluated in the way described in sects. 3.4, 4.1 and 4.2. The final results are presented in table 1. The errors include statistical contributions and uncertainties connected with the cascade feeding and side-feeding as well as with inaccuracies of the stopping-power parameters.

5.1 The $I^\pi = 43/2^-$, $39/2^-$, $35/2^-$, $27/2^-$ and $23/2^-$ levels

For transitions from the $43/2^-$, $39/2^-$, $35/2^-$ levels lineshape analysis of the "sum" spectra was made by the "gating below" techniques. The resulting DSAM lineshapes are almost symmetrical since the spectra from all detectors were summed. The lifetimes of the $43/2^-$, $39/2^-$ levels were obtained from two-dimensional fits of the lineshapes performed with the free parameters τ and Q_{high}. The errors given in table 1 include uncertainties of Q_{high}. In the case of $35/2^-$, $27/2^-$ and $23/2^-$ levels the statistical errors were determined as 0.04, 0.08 and 0.15 ps, respectively. The total errors, given in table 1, have been increased due to cascade and side-feeding uncertainties. As an example the lineshape analysis for the 985 keV transition depopulating the $35/2^-$ level is shown in fig. 8. Figures 9 and 10 illustrate the lineshape analysis for the 793 keV and 672 keV transitions depopulating the $27/2^-$ and $23/2^-$ levels, respectively. In the case of $23/2^-$ and $27/2^-$ levels the intensity was sufficient for lineshape analysis at selected angles, 38° and 142°. In the case of the 672 keV line the Doppler effect is weak because of long lifetime and strong cascade feeding (see appendix B). Nevertheless the Doppler tail is visible and the lineshape analysis is still possible due to the favourable background and large statistics. The lifetime 1.47 ps for the $23/2^-$ level was obtained assuming that only a part of the DSF with $U > 0.5\,\mathrm{MeV}$ is taken into account. For two extreme hypotheses of side-feeding (CSF and CSF+DSF) lifetimes of 1.71 ps and 1.23 ps were obtained. Hence the maximum uncertainty connected with side-feeding calculations is equal to ± 0.24 ps. This value together with the statistical error and the uncertainty of the stopping power gives the final error shown in table 1.

Table 1. Lifetimes and $B(E2; I \to I-2)$ values for the levels in the yrast band of ^{131}La.

I	τ (ps)[a]	τ (ps)[b]	$B(E2)^a$ (e^2b^2)	Comments
$43/2^-$	0.33 ± 0.09		0.16^{+6}_{-3}	gate below, $336+533+672+793+901+985$; sum[d]
$39/2^-$	0.48 ± 0.11		0.13^{+4}_{-2}	gate below, $672+793+901+985$ and 901+984; sum[d]
$35/2^-$	0.47 ± 0.09		0.19^{+5}_{-3}	gate below, $336+533+672+793$; "38°"[e], "142°"[e], sum[d]
$31/2^-$	0.52 ± 0.13[c]	0.5 ± 0.4	0.26^{+9}_{-5}	gate below, $336+533+672+793$, gate above, narrow gate;"38°"[e], "142°"[e], sum[d]
$27/2^-$	0.75 ± 0.20	0.5 ± 0.4	0.35^{+13}_{-7}	gate below, $336+533+672$; "38°"[e], "142°"[e]
$23/2^-$	1.47 ± 0.35	1.2 ± 0.5	0.41^{+13}_{-8}	gate below, $336+533$; "38°"[e], "142°"[e]

[a] Obtained in the present work.
[b] Taken from ref. [3].
[c] The error accounts for the intensity uncertainties of contamination lines.
[d] Sum of spectra from all 10 detectors.
[e] "38°" —sum of the 25° and ±38° detectors, "142°" —sum of the ±142° and 155° detectors.

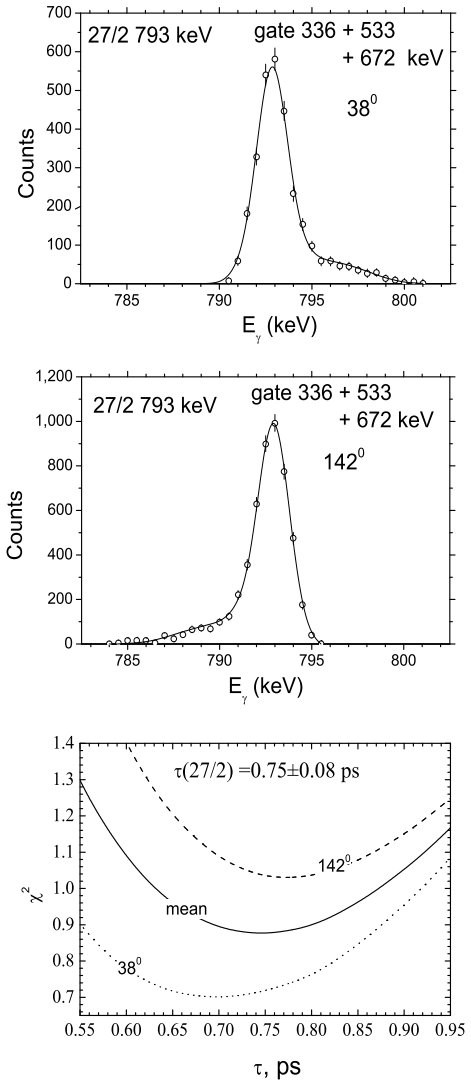

Fig. 9. Lifetime evaluation of the $27/2^-$ level by using the "gating below" method. See also caption to fig. 8. Only statistical errors are given.

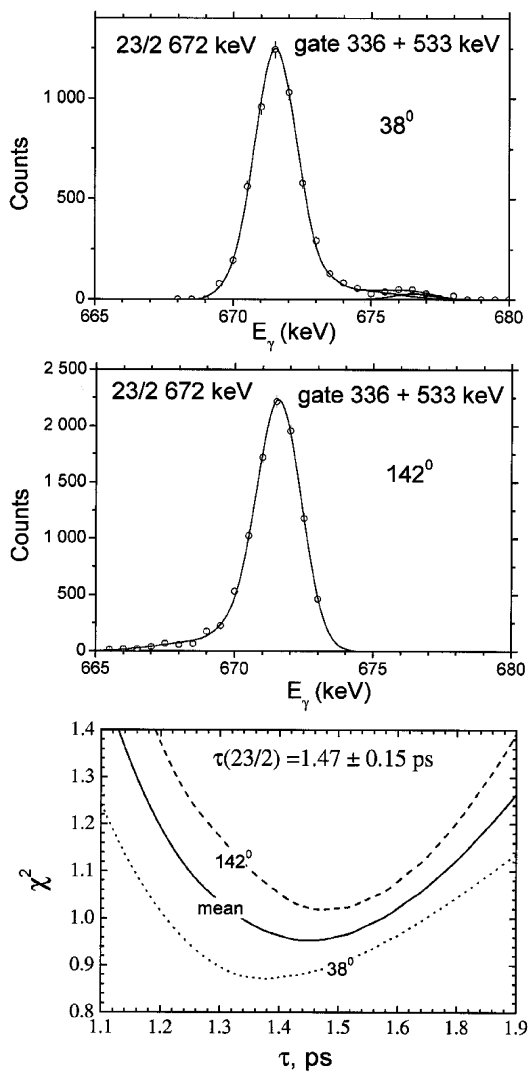

Fig. 10. Lifetime evaluation of the $23/2^-$ level by using the "gating below" method. See also caption to fig. 8. Only statistical errors are given.

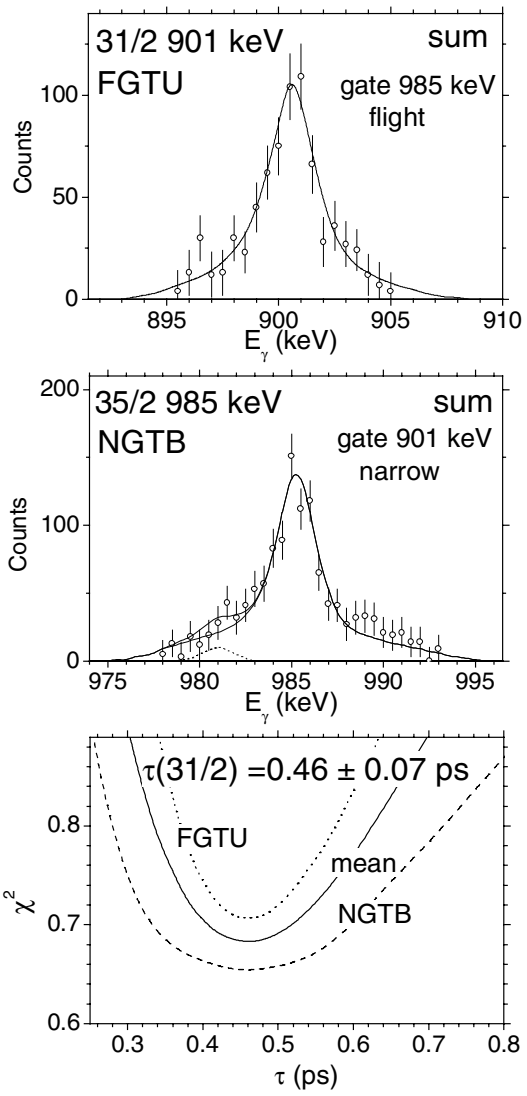

Fig. 11. Lifetime evaluation of the $31/2^-$ level by the methods independent of the cascade and side-feeding pattern details. Upper part: lineshape analysis, for the 901 keV transition depopulating the $31/2^-$ level, performed by using the "gating above" method (gate 985 keV, flight). Middle part: lineshape analysis, for the 985 keV transition depopulating the $35/2^-$ level, observed in the spectrum obtained with a narrow gate (901 ±1 keV, "narrow gate" method). Lower part: for comments on the χ^2 plot and background line see fig. 8.

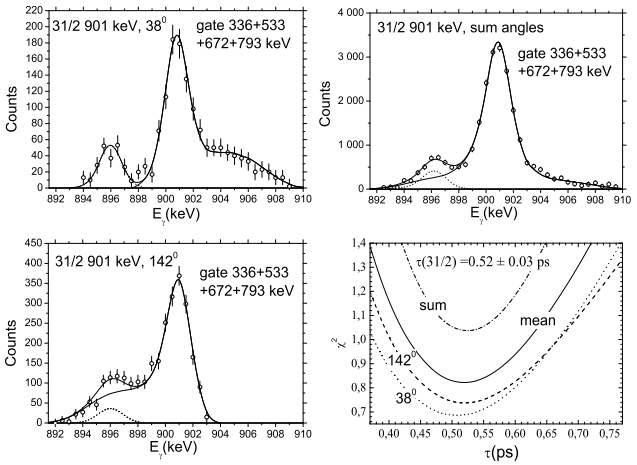

Fig. 12. Lifetime evaluation of the $31/2^-$ level by using the "gating below" method. See also caption to fig. 8. Only statistical errors are given.

5.2 The $I^\pi = 31/2^-$ level

Lineshape analysis of the $31/2^- \rightarrow 27/2^-$ transition has been made by using the "sum" spectrum and the spectra collected at angles: 38° and 142°. In addition to the "gating below" technique, the "gating above" and "narrow gate" methods have also been used (see fig. 11). The latter two methods are independent of the cascade and side-feeding pattern. Lineshape analysis of the 901 keV transition from the $31/2^-$ level, performed by using the "gating above" method, is shown in the upper part of fig. 11. Since the "sum" spectrum was analysed the gates were set in energy intervals of 978–983 keV and 987–992 keV which correspond to the "flight" component of the 985 keV line. The lineshape of the 985 keV transition depopulating the $35/2^-$ level, observed in the spectrum gated on 901 ±1 keV ("narrow gate" method) is presented in the middle of fig. 11. The evaluation of the lifetime of the $31/2^-$ level by the "gating below" method is shown in fig. 12.

It follows from figs. 11 and 12 that the lifetime obtained using the "gating below" method is in excellent agreement with those obtained by applying the "gating above" and "narrow gate" methods. This fact confirms that all feedings were correctly taken into account. The statistical errors resulting from the "gating above" and "narrow gate" methods (fig. 11) are larger than the statistical error obtained in the "gating below" method. This is due to the relatively weak intensities of the analysed γ-lines. However, if in the "gating below" method the uncertainties in the side and cascade feedings are taken into account then the total accuracy become comparable with the results of the "gating above" and "narrow gate" methods. In the case, when the use of the "gating above" and/or "narrow gate" techniques is possible, both methods should be employed as a good check of the results obtained by the "gating below" method. This gives us also the opportunity to check whether the unknown feedings are properly estimated.

6 Discussion

6.1 CQPC calculations for negative-parity states

The properties of the ^{131}La nucleus have been studied in terms of the Core-Quasi-Particle Coupling model (CQPC) [24–26]. In this model, the odd-A nucleus is considered as a quasi-particle coupled to the $(A-1)$ and $(A+1)$ even-even cores. In the case of $^{131}_{57}$La the valence 57th proton (particle) is coupled to the neighbouring $^{130}_{56}$Ba nucleus, whereas the proton-hole is coupled to

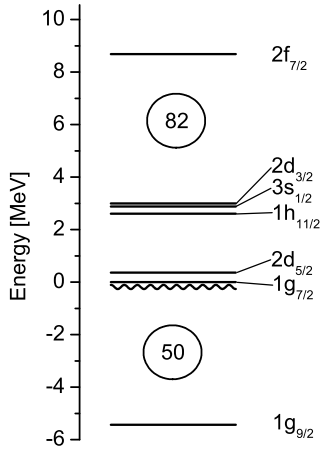

Fig. 13. Single-proton states in the Woods-Saxon spherical potential. The wavy line shows the position of the Fermi level.

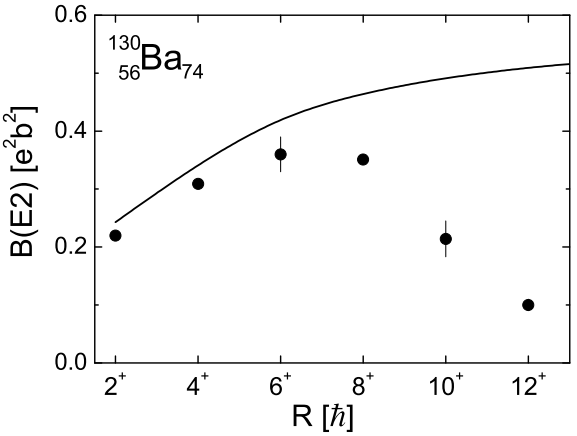

Fig. 14. Comparison of the calculated $B(E2;\ R \to R-2)$ values with the experimental data [29] for the yrast states in ^{130}Ba.

$^{132}_{58}$Ce. The quadrupole-quadrupole (q-Q) interaction between the quasi-particle and the core, as well as the pairing interaction are included in the model. In these calculations the q-Q interaction with strength $\chi = -9\,\mathrm{MeV}$ was used which is close to the theoretical value $\chi = -9.5\,\mathrm{MeV}$ [27]. For the gap parameter the standard formula $\Delta = 135/A\,\mathrm{MeV}$ was applied and the position of the Fermi level (see fig. 13) was chosen to reproduce the number of valence protons. Single-proton states (fig. 13) were generated from the Woods-Saxon spherical potential by using a standard set of parameters. The $1h_{11/2}$ and $2f_{7/2}$ proton states were taken into account to describe the negative-parity states in ^{131}La.

In our calculations 44 core states up to spin 16 were taken into account. The data (spin R, excitation energy $E(R)$ and reduced matrix elements $\langle R||E2||R'\rangle$) were taken from the Davydov-Filippov model (3-axial rigid rotor) [28]. To simplify the CQPC calculations it was assumed that the $(A-1)$ and $(A+1)$ cores have the properties of the real ^{130}Ba nucleus. The structure of the wave functions, obtained from the CQPC model, for negative-parity states of ^{131}La justifies this simplification. The parameters describing the ^{130}Ba nucleus in terms of the Davydov-Filippov model were: $\beta = 0.22$ (based on the $B(E2; 2^+ \to 0^+)$ value [29]), $\gamma = -24°$ (Lund convention) and $E(2^+) = 0.30\,\mathrm{MeV}$. The calculated $B(E2; R \to R-2)$ values for the ground-state band in ^{130}Ba are compared for this set of parameters with the experimental data in fig. 14. One can see that the Davydov-Filippov model does not reproduce well the $B(E2)$ values for spin $R \geq 8$. A significant drop in the $B(E2)$ values observed in the experiment [29] for $R > 8$ may be the result of band crossing. This effect cannot be reproduced in the frame of the Davydov-Filippov model which assumes rigid nucleus rotation with a fixed moment of inertia. The electromagnetic properties of the ^{131}La nuclei were calculated for the bare proton charge ($e^{eff} = e$) and for standard values of the effective orbital and spin g-factors ($g_p^{(l)} = 1$, $g_p^{(s)} = 0.6\ g_p^{(s)free}$).

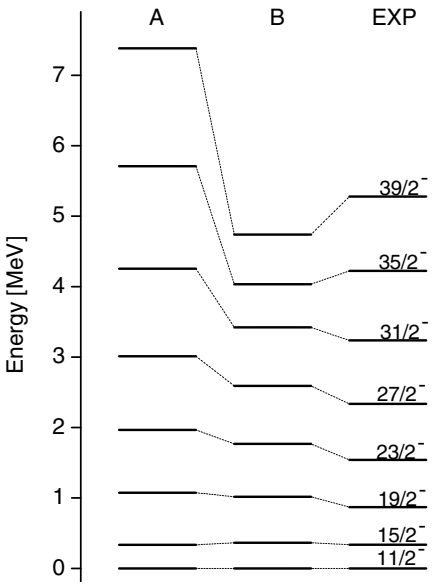

Fig. 15. Comparison of the experimental level scheme of ^{131}La [2] with the results of the CQPC model calculation. Only the part of the negative-parity level scheme relevant to our discussion is shown. A: All properties of the ^{130}Ba core have been taken from the Davydov-Filippov model. B: The phenomenological core (see text) has been used. The energy of the $(11/2^-)_1$ state was set equal to 0.

The results of the CQPC calculations show that the yrast negative-parity band in ^{131}La is mainly built on the $1h_{11/2}$ proton state while the contribution of the $2f_{7/2}$ state is of minor significance. It was also found that the main terms of the wave function for the discussed levels ($11/2^-$, $15/2^-$, ..., see fig. 1) in ^{131}La consist of the ^{130}Ba yrast states. The predicted properties of ^{131}La are compared with the experimental data in figs. 15 and 16. Considerable disagreement between the calculated and experimental $B(E2)$ values is observed for $I^\pi \geq 27/2^-$. Note that the $27/2^-$ state is mainly built on the proton $1h_{11/2}$ configuration coupled to the core state with spin $R = 8$. Above that state the theoretical $B(E2)$ values for ^{130}Ba differ significantly from the experimental

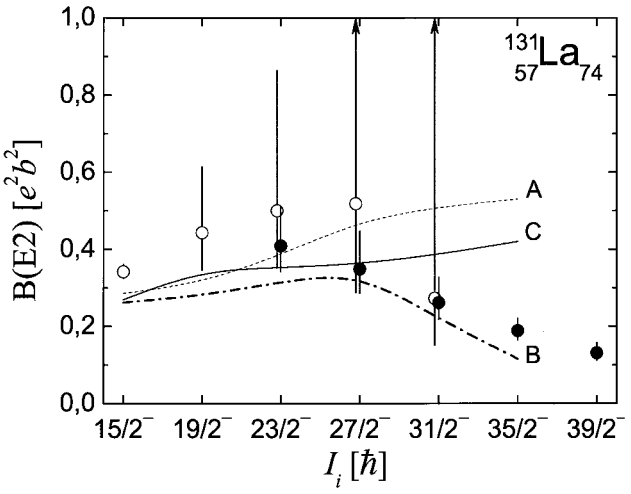

Fig. 16. Observed and calculated $B(E2;\ I \to I-2)$ values for the $\pi h_{11/2}$ decoupled band in ^{131}La. The meanings of A and B are the same as in fig. 15; C: results of the TRS calculations. Full and open circles denote the results of our experiment and data from ref. [3], respectively.

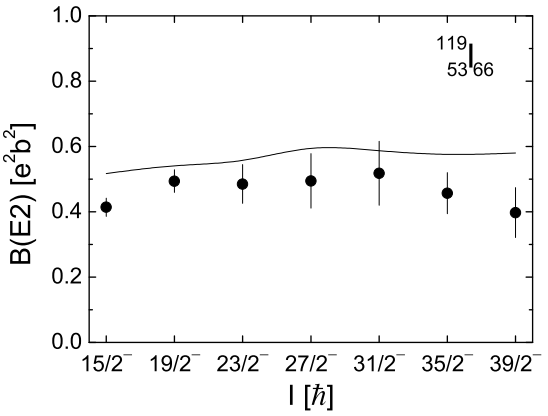

Fig. 17. Comparison of the experimental $B(E2;\ I \to I-2)$ values for the $\pi h_{11/2}$ decoupled band in ^{119}I [7] with the results of the TRS calculations.

ones (fig. 14). The calculation shows that the rigid rotor model is unable to reproduce the properties of the high-spin states in ^{131}La. One can see that changes which occur in high-spin states of the even-even core of ^{131}La should be taken into account. Therefore, in the next step, the experimental level energies of ^{130}Ba and experimental values of the $\langle R||E2||R-2\rangle$ matrix elements corresponding to the $B(E2; R \to R-2)$ values [29,30] shown in fig. 14 were applied as input data for $R^\pi \leq 12^+$ in the CQPC calculations. Theoretical values were used in the cases for which the experimental data were not available. The core with such properties will be called phenomenological. The calculations of ^{131}La were limited to spin $I = 35/2$ built of $R = 12$ and $j = 11/2$.

The CQPC calculations involving the phenomenological core give much better results (see figs. 15 and 16) than when the theoretical 3-axial rigid core is used. In particular, they qualitatively reproduce the decrease of $B(E2)$ values for spins $I > 27/2$. We conclude that the electromagnetic properties of the ^{130}Ba core have a strong influence on the $E2$ transition probabilities in the decoupled band in ^{131}La.

6.2 TRS calculations

Additional calculations were preformed in terms of the Self-Consistent Total Routhian Surface (SC-TRS) model (see ref. [26] and references therein). The Hamiltonian in this model is based on the deformed Woods-Saxon potential involving the Strutinsky shell correction formalism with the monopole and quadrupole pairing interactions included. The Routhian was calculated on a grid in the non-axial quadrupole deformation space (β_2, γ) including the hexadecapole (β_4) degrees of freedom. The Routhian was minimised with respect to the shape parameters to obtain equilibrium deformations.

The TRS calculations show that the ^{131}La nucleus is very soft to γ deformation and the positions of minima change from $\gamma \approx 22°$ (Lund convention) at the beginning of the band ($\hbar\omega \simeq 0.18\,\mathrm{MeV}$) to $\gamma \approx -20°$ at $\hbar\omega \simeq 0.58\,\mathrm{MeV}$. Simultaneously, the equilibrium deformation parameter β_2 decreases slightly from 0.20 to 0.18. Calculations predict that the configuration of the quasi-proton wave function changes from an almost pure $K = 1/2$ for low-energy states (up to $\hbar\omega \simeq 0.3\,\mathrm{MeV}$) to a mixed $K = 3/2$ and $K = 5/2$ configuration for higher-energy states (with $\hbar\omega \geq 0.3\,\mathrm{MeV}$). The transition probability $B(E2)$ in the yrast band can be roughly estimated [31] from the equation

$$B(E2; I_i \to I_f) = \frac{5}{16\pi} Q_t^2 \langle I_i K 20 | I_f K\rangle^2, \qquad (7)$$

where Q_t is the transition quadrupole moment which within the limits of a large angular momentum [32] is

$$Q_t = Q_{20} + \sqrt{\frac{2}{3}} Q_{22}\,. \qquad (8)$$

The quantities Q_{20} and Q_{22} are the components of the quadrupole moment. In eq. (7) the value of K of the dominant part of the wave function was used, whereas Q_{20} and Q_{22} were obtained from the TRS model. Note that Q_{22} used in ref. [32] and in this paper differs from the standard definition (see, *e.g.*, [33]). Our Q_{22} equals $\sqrt{2}Q_{22}$ used in [33].

The TRS calculation (for the results see fig. 16) does not reproduce the experimental $B(E2; I \to I-2)$ values for $I > 27/2$. One reason for the observed discrepancy is that in the TRS model one does not calculate the matrix elements of Q_{20} and Q_{22} between the initial (with spin I) and final (with spin $I-2$) states. Therefore, formulae (7) and (8) give only an approximate value of the $E2$ transition probability if the initial and final states have different configurations.

Among nuclei belonging to the $50 < Z,\ N < 82$ region we have the case of ^{119}I in which the experimental

$B(E2)$ values for the $h_{11/2}$ proton band are nearly constant (fig. 17) for $15/2^- \leq I \leq 39/2^-$ [7]. The TRS calculation carried out for this band predicts that the quadrupole deformation $\beta_2 \approx 0.29$, $\gamma \approx 10°$ and the $h_{11/2}$ quasi-proton configuration (with the main $K = 1/2$ component) do not vary with spin value (for $I \leq 16$). Therefore, the conditions to apply eqs. (7) and (8) are fulfilled and the theory reproduces the observed dependence of $B(E2)$ *vs.* I (see fig. 17).

7 Summary

Lifetimes of levels belonging to the $\pi h_{11/2}$ band in ^{131}La have been measured by the DSA method. Different gating conditions: "gating below", "gating above" and "narrow gate" have been applied. The model of side-feeding population is presented and experimentally tested. The experimental $B(E2)$ values for intraband transitions between levels with spin $I \leq 35/2^-$ have been compared with the results of theoretical calculations made in terms of the CQPC and TRS models. None of these models can reproduce the diminishing value of $B(E2)$ for spin values above $27/2^-$. Only a phenomenological approach made in the frame of the CQPC model and based on experimental energies and $B(E2)$ values of ^{130}Ba allows for fairly good reproduction of experimental data. One can conclude that for proper interpretation of the chiral bands in the neighbouring odd-odd ^{130}La and ^{132}La a good understanding of the simpler structure of even-odd nuclei, like ^{131}La, is very important.

We are grateful to the staff of the Warsaw Cyclotron for the excellent beam provided during the experiment and to A. Stolarz for the preparation of targets. The authors acknowledge the very fruitful discussions with Professors J. Dobaczewski, S.G. Rohoziński, W. Satuła and A. Marcinkowski.

Appendix A. The "narrow gate" method (NGTB)

The "narrow gate" method [14] allows the evaluation of lifetimes when a narrow gate is set on the unshifted component of the transition depopulating the level of interest while the lineshape of the transition feeding this level is analysed. The small velocity of recoils in our reaction ($\approx 1\%c$) causes that the maximal Doppler shift (ΔE_γ^{max}) is comparable with the FWHM of the instrumental line (for $E_\gamma \approx 1\,\mathrm{MeV}$ the value of FWHM $\approx (1/6)\Delta E_\gamma^{max}$). When the spectra registered by detectors placed at different angles are summed it is practically impossible to achieve the ideal "narrow gate" case (fig. 18), in which the gate is set only on the stopped component of the "transition below". The improved version of this method [10] may be applied for any gate width. Figure 18 shows the attenuation factor $F(\tau)$ describing the usefulness of the "narrow gate" method in the cases of different widths of

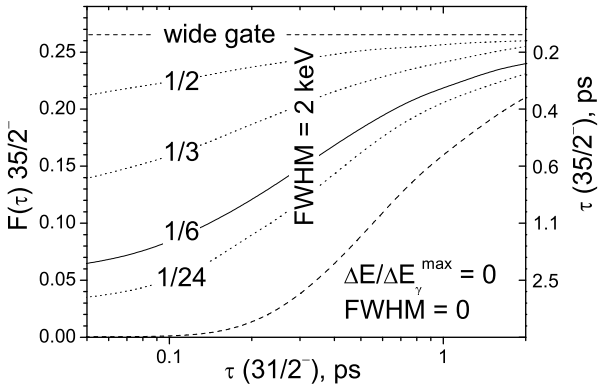

Fig. 18. Sensitivity of the "narrow gate" method for different $\Delta E/\Delta E_\gamma^{max}$ ratios, where ΔE is the gate width and ΔE_γ^{max} is the maximum Doppler shift. The gates are set on the 901 keV transition. Dashed lines present two extreme cases: one when the width of the gate ΔE is very large and one when $\Delta E = 0$ and FWHM = 0 keV (ideal case). The solid line shows the real experimental conditions with the gate set at 901 ± 1 keV ($\Delta E/\Delta E_\gamma^{max} = 1/6$ since $\Delta E_\gamma^{max} = 12$ keV) and FWHM = 2 keV. The $\Delta E/\Delta E_\gamma^{max} = 1/24$ curve corresponds to the experimental limit, when $\Delta E = 0.5$ keV.

gates set on the 901 keV transition de-exciting the studied $31/2^-$ level. The quantity $F(\tau)$ is defined as

$$F(\tau) = \langle \Delta E_\gamma \rangle / \Delta E_\gamma^{max}, \tag{A.1}$$

where τ denotes the lifetime of the level (in our case it is the $35/2^-$ level), $\langle \Delta E_\gamma \rangle$ and ΔE_γ^{max} are related to the average velocity of recoils just at the moment of γ-emission and the velocity of recoils just after they are formed, respectively. Note that the observed value of $F(\tau)$ for the $35/2^-$ level decay depends on the gate width set on the $31/2^- \rightarrow 27/2^-$ transition since the gate chooses the range of recoil velocity at the moment of γ-ray emission. The slope of the $F(\tau)$ curve is the measure of sensitivity for lifetime determination.

Two extreme cases are considered: one when the width of the gate (ΔE) is very large and the second one when ΔE and FWHM of the apparatus lineshape are zero (ideal "narrow gate"). The curve for $\Delta E/\Delta E_\gamma^{max} = 1/24$ corresponds to the experimental limit when $\Delta E = 0.5$ keV (*i.e.* one channel at 0.5 keV/channel calibration). As one can see that, even for a gate width of one channel ($\Delta E = 0.5$ keV), the experimental conditions are far from the ideal "narrow gate" case. This is explained by the relatively low initial recoil velocity in our reaction ($\approx 1\%$ c). In the case of ref. [10], where the initial recoil velocity was $\approx 2.5\%$ c even for the gate width $\Delta E = 2 \times$ FWHM the sensitivity of the "narrow gate" analysis decreases only a little as compared with the ideal case. On the other hand, fig. 18 shows that the increase of gate width up to $\Delta E = 2$ keV (solid line) has no noticeable influence on the sensitivity of the "narrow gate" method as compared with $\Delta E = 0.5$ keV (compare $F(\tau)$ curves for $\Delta E/\Delta E_\gamma^{max} = 1/6$ and $1/24$). One can conclude from fig. 18 that in the discussed case, the "narrow gate" analysis is effective only if the lifetime of the $31/2^-$ level lies

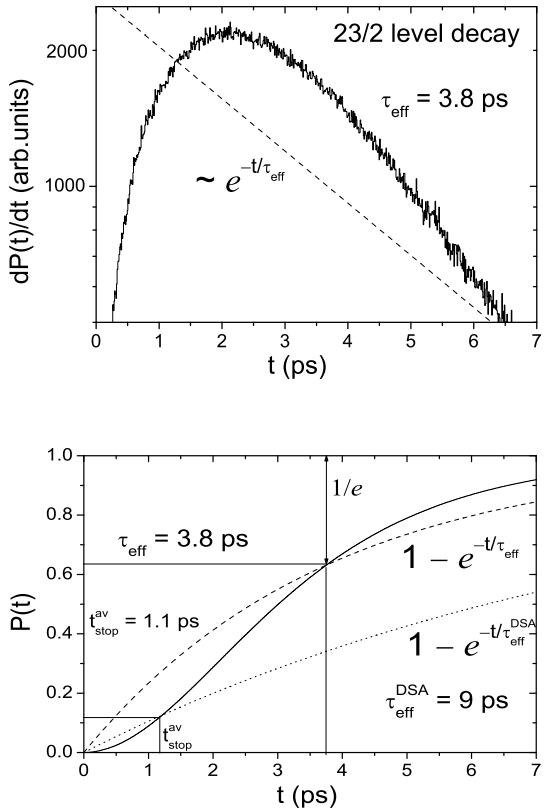

Fig. 19. The differential (upper) and integral (lower) decay functions for the 23/2 level. The histogram in the upper part presents the number of decay (from Monte Carlo simulation) as a function of time. This quantity is proportional to $\mathrm{d}P/\mathrm{d}t$. The ordinate is given in a logarithmic scale. The corresponding integral function is shown in the lower part of the figure as a solid line. Dashed lines in both pictures show the simple exponential dependence with $\tau = \tau_{eff}$. The value of $\tau_{eff} = 3.8\,\mathrm{ps}$ follows from the $P(t)$ *vs.* t curve. Dotted line shows the exponential approximation with $\tau = \tau_{eff}^{DSA}$.

in the range 0.15 ps to 0.6 ps and $F(\tau)$ of the $35/2^-$ level decay is in the range 0.1 to 0.2 (which is equivalent to the lifetime of the $35/2^-$ level in the range 1.1 ps to 0.4 ps). From the point of view of statistics a wide gate is advantageous, but on the other hand, it results in a decrease of sensitivity of lifetime evaluation.

Appendix B. Effective lifetimes in DSAM

For complicated level decay the effective lifetime τ_{eff} can be introduced. It is defined by the equation

$$\int_0^{\tau_{eff}} (\mathrm{d}P(t)/\mathrm{d}t)\mathrm{d}t = 1 - e^{-1},$$

similarly to the standard definition for effective $T_{1/2}$: $\int_0^{T_{1/2}} (\mathrm{d}P(t)/\mathrm{d}t)\mathrm{d}t = 1/2$. For the 23/2 level the decay function $\mathrm{d}P/\mathrm{d}t$, which takes into account all cascade and side-feeding components is shown in the upper part of fig. 19 by way of example. The histogram shown in this figure is the result of the Monte Carlo simulation. The corresponding integral function $P(t)$ is shown in the lower part of the figure as a solid line. In accordance with the proposed definition τ_{eff} equals 3.8 ps, which is close to the rough estimation of $\tau_{eff} \approx 4\,\mathrm{ps}$ (calculated as the sum of lifetimes in the cascade). The dashed lines in both figures show the simple exponential dependence for $\tau = \tau_{eff}$.

In the lifetime measurements by the DSA method the slowing-down process of recoils moving inside the target is taken into account. Using the stopping-power parameters given in sect. 3.5 we can calculate the time needed to fully stop (it means that their velocity decreases 100 times) the recoils, $t_{stop} \approx 1.8\,\mathrm{ps}$. In a similar way we define the average stopping time t_{stop}^{av} as the time which is needed to reduce the velocity by a factor e [34] (in our case $t_{stop}^{av} \approx 1.1\,\mathrm{ps}$). For an ideal γ-detector the ratio of the Doppler tail intensity to the total γ-line intensity is $P(t_{stop})$. For γ-detectors with FWHM > 0 the observed Doppler-shifted fraction is always smaller and roughly corresponds to $P(t_{stop}^{av})$. Thus, from the point of view of the Doppler effect, the effective lifetime τ_{eff}^{DSA}, which is defined using the formula $P(t_{stop}^{av}) = (1 - e^{-t_{stop}^{av}/\tau_{eff}^{DSA}})$, always exceeds τ_{eff} if the decay curve differs from the exponential one. In our case $\tau_{eff}^{DSA} \approx 9\,\mathrm{ps}$. The corresponding exponential approximation is shown in the lower part of fig. 19 as dotted line. In spite of the fact that $\tau_{eff}^{DSA} \approx 9\,\mathrm{ps}$, $\tau_{eff} \approx 4\,\mathrm{ps}$ and $t_{stop}^{av} \approx 1\,\mathrm{ps}$ it is possible to extract the lifetime because even in this case the Doppler tail fraction ($\approx 10\%$) is still measurable.

Summarising, for τ_{eff} larger or comparable with the recoil stopping time the effective lifetime τ_{eff}^{DSA} can significantly exceed τ_{eff}. Even then there is a possibility of measuring the lifetime when the statistics is high enough (see the χ^2 plot in fig. 10).

Appendix C. Calculation of side-feeding γ-cascades

The entry-state distribution has been simulated basing on the statistical theory of nuclear reactions. The improved version of the Monte Carlo code COMPA (intended also for the simulation of recoil kinematical parameters) was used for the Doppler γ-lineshape analysis [7,21]. The dependence of transmission coefficients $T_L(E)$ on the input angular momenta L can be calculated from the optical model [35] in two versions where:

1) the effective-interaction radius corresponds to the grazing collision, *i.e.* $R_{inter} = R_{grazing}$;

2) the empirical correction factor $f_c < 1$ is introduced, *i.e.* $R_{inter} = f_c \times R_{grazing}$. This factor mainly influences the maximal input angular momenta and can be determined by comparing the calculated cross-sections for compound-nucleus formation ($\sigma_c \sim \sum_L (2L+1)T_L$) with the experimental value σ_e. In the lack of experimental data the value of σ_e can be found from an empirical formulae [36].

In the present work the level density parameters have been chosen in accordance with modern systematics [37].

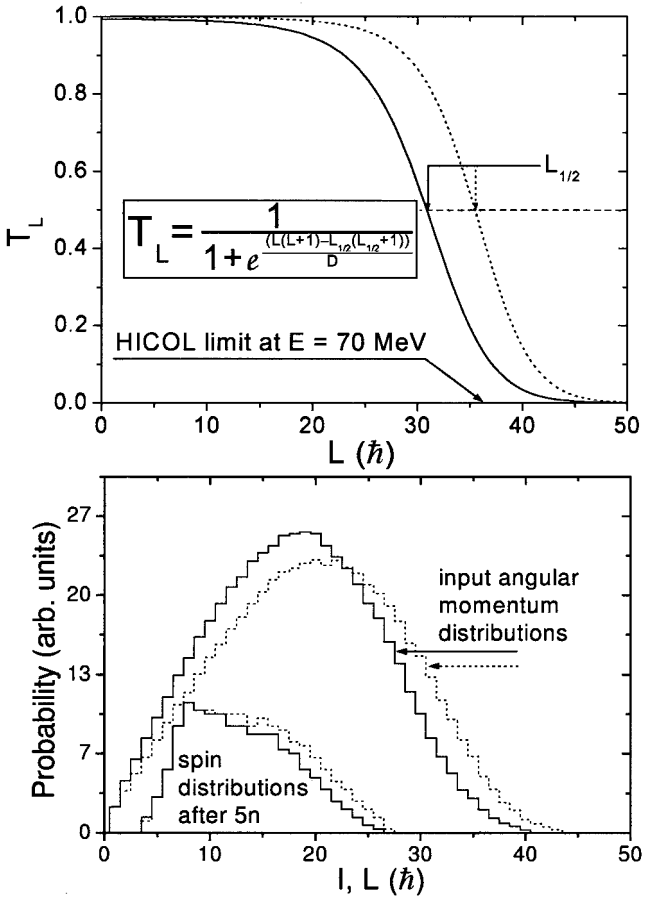

Fig. 20. Results of calculations for the ^{122}Sn(^{14}N, 5n) reaction at $E = 70$ MeV. Upper part: transmission coefficients T_L calculated for ^{14}N bombarding the ^{122}Sn target. The appropriate formula is given in inset. The dotted curve corresponds to the two-parameters approximation of the optical model [35]. Parameters $D = 196$ and $L_{1/2} = 35.4$ were used. The solid line shows the results of calculation obtained when the based on systematics experimental fusion cross-sections [36] was taken into account. The dynamical limit of compound-nucleus formation, calculated by the code HICOL [39] is marked by an arrow. Lower part: distribution of the input angular momentum in the ^{136}La compound nucleus and spin distribution (after 5 neutron evaporation) with (solid line) and without (dotted line) account taken of the experimental systematics of fusion cross-section. The Monte Carlo calculations have been made for a thick target (10 mg/cm^2), with account being taken of the slowing-down process of the bombarding particles.

The competition between the particle evaporation and γ-ray emission is evaluated basing on the systematics of the $E1$ strength functions [38]. Transmission coefficients T_L calculated for the reaction ^{122}Sn + ^{14}N at $E = 70$ MeV are presented in the upper part of fig. 20. The dotted curve relates to the two-parameter approximation of the optical model ($f_c = 1$), whereas the solid line relates to the corrected version ($f_c = 0.87$). The dynamical limit of compound-nucleus formation, calculated by the code HICOL [39] is marked by the arrow. Two distributions of the input angular momenta and spins after evaporation of 5 neutrons, calculated for $f_c = 1$ and $f_c = 0.87$, are shown in the lower part of fig. 20. These calculations have been made for a thick target, with account being taken of the slowing-down process of the bombarding particles. Unlike the cases with evaporation of two or three neutrons, the differences in the input angular-momenta distribution slightly influences the spin distribution in the 5n channel (lower part of fig. 20). It is so because reactions with 5 neutrons evaporation occur from the low and middle regions of the input angular momenta distribution. Therefore, the uncertainty in semi-empirical evaluation of T_L cannot remarkably affect the entry-state population distribution. Calculation of the fission barrier $B(L)$ [40,41] gives $L_f \approx 66\hbar$ (which corresponds to the fission barrier equal to the neutron binding energy $B(L_f) = B_n \approx 8$ MeV). This value exceeds the angular momenta involved in our reaction. Therefore, the fission phenomenon does not play an important role in our case. The distribution of the entry-state population in ^{131}La calculated with corrected T_L is presented in fig. 2.

The decay of entry states via quasi-continuum γ-quanta is calculated by using the Monte Carlo method [18, 19]. Usually, it is assumed that the side-feeding pattern is defined by the competition between stretched $E2$ transitions (including the rotational damping effect [42]) and the statistical $E1$ transitions. In our calculations the statistical $M1$ and $E2$ transitions are also taken into account. The parameters for calculating the statistical γ-transitions have been chosen in accordance with modern systematics of $E1$ Dipole, $M1$ Spin-flip and $E2$ Quadrupole Giant Resonances [38]. For low- and high-spin states the contribution of $E2$ stretched cascades can be calculated with different effective quadrupole moments Q_{low} and Q_{high}. The damping effect is calculated for the width $\Gamma = 0.3$ MeV. Another effect, typical for weakly deformed nuclei, is the presence of magnetic rotational bands with shears effects [23,43]. In our calculations the existence of magnetic rotational bands in continuum was also taken into consideration. In refs. [18,19] the density of stretched magnetic bands is described by a special parameter S_{MR} responsible for the contribution of $M1$ stretched cascades to the total decay strength. For medium and low spin levels of the yrast band in ^{131}La the influence of Q_{low} and stretched $M1$ transitions becomes important and results in a remarkable delay of the side-feeding population. The value of Q_{high} is expected to be large [23], whereas Q_{low} should be much smaller than Q_{high}. It follows from the systematics of $B(E2)$ values in the $A \approx 130$ mass region that $Q_{low} \approx 3$–6 eb. The parameter S_{MR} has been evaluated only for near-magic and transitional isotopes of Gd, Eu and Sm [19,44] basing on multiplicity distribution analysis and turns out to be $S_{MR} \approx 0.02$–0.1. It is expected that the S_{MR} value for ^{131}La should also lie in this range.

References

1. K. Starosta, C.J. Chiara, D.B. Fossan, T. Koike, T.T.S. Kuo, D.R. LaFosse, S.G. Rohoziński, Ch. Droste, T. Morek, J. Srebrny, Phys. Rev. C **65**, 044328 (2002).
2. L. Hildingsson, C.W. Beausang, D.B. Fossan, R. Ma, E.S. Paul, W.F. Piel jr., N. Xu, Phys. Rev. C **39**, 471 (1989).

3. N.V. Zamfir, A. Dewald, K.O. Zell, P. von Brentano, Z. Phys. A **344**, 21 (1992).
4. E. Grodner, Ch. Droste, T. Morek, J. Srebrny, A.A. Pasternak, A. Wasilewski, W. Płóciennik, E. Ruchowska, *Proceedings of the XXXVII Zakopane School Of Physics*, Acta Phys. Pol. B **34**, 2447 (2003).
5. T.K. Alexander, J.S. Foster, *Advances in Nuclear Physics*, edited by M. Baranger, E. Vogt, Vol. **10** (Plenum Press, New York, London, 1978) p. 197.
6. K.P. Lieb, in *Experimental Techniques in Nuclear Physics*, edited by D.N. Poenaru, W. Greiner (Walter de Gruyter, Berlin, New York, 1997) p. 425.
7. J. Srebrny, Ch. Droste, T. Morek, K. Starosta, A.A. Wasilewski, A.A. Pasternak, E.O. Podsvirowa, Yu.N. Lobach, G.B. Hagemann, S. Juutinen, M. Piiparinen, S. Törmanen, A. Virtanen, Nucl. Phys. A **683**, 21 (2001).
8. J.C. Wells, N. Johnson, *Lineshape: a computer program for Doppler-broadened lineshape lifetime analysis*, Report No. ORNL-6689, 1991, p. 44.
9. F. Brandolini, M. Ionescu-Bujor, N.H. Medina, R.V. Ribas, D. Bazzacco, M. De Poli, P. Pavan, C. Rossi Alvarez, G. de Angelis, S. Lunardi, D. De Acuna, D.R. Napoli, S. Frauendorf, Phys. Lett. B **388**, 468 (1996).
10. R.M. Lieder, A.A. Pasternak, E.O. Podsvirova, A.D. Efimov, V.M. Mikhajlov, R. Wyss, Ts. Venkova, W. Gast, H.M. Jäger, L. Mihailescu, D. Bazzacco, S. Lunardi, R. Menegazzo, C. Rossi Alvarez, G. de Angelis, D.R. Napoli, T. Rzaca-Urban, W. Urban, A. Dewald, Eur. Phys. J. A **21**, 37 (2004).
11. E.O. Podsvirova, R.M. Lieder, A.A. Pasternak, S. Chmel, W. Gast, Ts. Venkova, H.M. Jäger, L. Mihailescu, G. de Angelis, D.R. Napoli, A. Gadea, D. Bazzacco, R. Menegazzo, S. Lunardi, W. Urban, Ch. Droste, T. Morek, T. Rzaca-Urban, G. Duchene, Eur. Phys. J. A **21**, 1 (2004).
12. A.A. Pasternak, E.O. Podsvirova, R. M. Lieder, S. Chmel, W. Gast, Ts. Venkova, H.M. Jäger, L. Mihailescu, G. de Angelis, D.R. Napoli, A. Gadea, D. Bazzacco, R. Menegazzo, S. Lunardi, W. Urban, Ch. Droste, T. Morek, T. Rzaca-Urban, G. Duchene, A. Dewald, Eur. Phys. J. A **23**, 191 (2005).
13. P. Petkov, D. Tonev, J. Gableske, A. Dewald, P. von Brentano, Nucl. Instrum. Methods A **437**, 274 (1999).
14. F. Brandolini, R. Ribas, Nucl. Instrum. Methods A **417**, 150 (1998).
15. P. Petkov, D. Tonev, A. Dewald, P. von Brentano, Nucl. Instrum. Methods A **488**, 555 (2002).
16. A.A. Pasternak, J. Srebrny, A.D. Efimov, V.M. Mikhailov, E.O. Podsvirova, Ch. Droste, T. Morek, S. Juutinen, G.B. Hagemann, M. Piiparinen, S. Törmanen, A. Virtanen, Eur. Phys. J. A **13**, 435 (2002).
17. A.A. Pasternak, Y. Sasaki, A.D. Efimov, V.M. Mikhajlov, T. Hayakawa, Y. Toh, M. Oshima, Y. Hatsukawa, J. Katakura, N. Shinohara, Z. Liu, K. Furuno, Eur. Phys. J. A **9**, 293 (2000).
18. A.A. Pasternak, R.M. Lieder, E.O. Podsvirova, W. Gast, H.M. Jäger, L. Mihailescu, D. Bazzacco, S. Lunardi, R. Menegazzo, C. Rossi Alvarez, G. de Angelis, D.R. Napoli, T. Rzaca Urban, W. Urban, Annual Report 2001, Laboratori Nazionali di Legnaro, Legnaro, p. 44, `www.lnl.inf.it`.
19. A.A. Pasternak, R.M. Lieder, E.O. Podsvirova, W. Gast, H.M. Jäger, L. Mihailescu, D. Bazzacco, S. Lunardi, R. Menegazzo, C. Rossi Alvarez, G. de Angelis, D.R. Napoli, K. Siwek-Wilczyńska, Annual Report 2002, Laboratori Nazionali di Legnaro, Legnaro, p. 17, `www.lnl.inf.it`.
20. I. Zalewska *et al.*, in preparation.
21. I.Kh. Lemberg, A.A. Pasternak, in *Modern Methods of Nuclear Spectroscopy* (Nauka, Leningrad, 1985) (in Russian).
22. J.F. Ziegler, J.P. Biersack, U. Littmark, *The Stopping Powers and Ranges of Ions in Matter*, Vol. **1** (Pergamon, New York, 1985); software TRIM1991, SRIM2000.
23. R.M. Clark, I.Y. Lee, P. Fallon, D.T. Joss, S.J. Asztalos, J.A. Becker, L. Bernstein, B. Cederwall, M.A. Deleplanque, R.M. Diamond, L.P. Farris, K. Hauschild, W.H. Kelly, A.O. Macchiavelli, P.J. Nolan, N. O'Brien, A.T. Semple, F.S. Stephens, R. Wadsworth, Phys. Rev. Lett. **76**, 3510 (1996).
24. F. Dönau, S. Frauendorf, J. Phys. Soc. Jpn. Suppl. **44**, 526 (1978).
25. F. Dönau, U. Hagemann, Z. Phys. A **293**, 31 (1979).
26. K. Starosta, Ch. Droste, T. Morek, J. Srebrny, D.B. Fossan, D.R. LaFosse, H. Schnare, I. Thorslund, P. Vaska, M.P. Waring, W. Satuła, S.G. Rohoziński, R. Wyss, I.M. Hilbert, R. Wadsworth, K. Hauschild, C.W. Beausang, S.A. Forbes, P.J. Nolan, E.S. Paul, Phys. Rev. C **53**, 137 (1996).
27. A. Arima, Nucl. Phys. A **354**, 19c (1981).
28. A. Davydov, G. Filippov, Nucl. Phys. **8**, 237 (1958).
29. O. Stuch, K. Jessen, R.S. Chakrawarthy, A. Dewald, R. Kühn, R. Krücken, P. Petkov, R. Peusquens, H. Tiesler, D. Weil, I. Wiedenhöver, K.O. Zell, P. von Brentano, C. Ender, T. Härtlein, F. Köck, O. Koschorrek, P. Reiter, Phys. Rev. C **61**, 044325 (2000).
30. B. Singh, Nucl. Data Sheets **93**, 33 (2001).
31. I. Hamamoto, Nucl. Phys. A **520**, 297c (1990).
32. P. Ring, A. Hayashi, K. Hara, H. Emling, E. Grosse, Phys. Lett. B **110**, 423 (1982).
33. A. Bohr, B.R. Mottelson, *Nuclear Structure*, Vol. **II** (Benjamin, Inc., 1975).
34. J. Lindhardt, M. Scharff, H.E. Schiott, Kgl. Dan. Vidensk. Selsk. Mat.-Fys. Medd. **33**, No. 14 (1963).
35. V.V. Babikov, JETP **38**, 264 (1960) (in Russian).
36. S. Kailas, S.K. Gupta, Z. Phys. A **302**, 355 (1981).
37. S.F. Mughabghab, C. Dunford, *On the Questions of the Nuclear Level Density and the E1 Photon Strength Functions*, Trans. Bulg. Nucl. Soc. **5**, 99 (2000).
38. J. Kopecky, in IAEA-TECDOC-1034, August 1998, Chapt. 6, `http://www-nds.iaea.org/reports-new/tecdocs/iaea-tecdoc-1034.pdf`.
39. H. Feldmeier, Rep. Prog. Phys. **50**, 915 (1987).
40. R. Vandenbosch, J.R. Huizenga, *Nuclear Fission* (Academic Press, New York and London, 1973).
41. A.J. Sierk, Phys. Rev. C **33**, 2039 (1986).
42. T. Dossing, E. Vigezzi, Nucl. Phys. A **587**, 513 (1995).
43. R.M. Clark, A.O. Macchiavelli, Annu. Rev. Nucl. Part. Sci. **50**, 36 (2000).
44. A.A. Pasternak, R.M. Lieder, E.O. Podsvirova, W. Gast, Acta Phys. Pol. B **36**, 1039 (2005).